Latrophilin 2 controls vascular morphogenesis and function by inhibiting endothelial cell adhesion and YAP/TAZ mechanosignaling

Chiara Camillo[1,2†], Nicola Facchinello[3], Dafne Gays[4], Giulia Villari[1,2], Noemi Gioelli[1,2], Chiara Sandri[1,2], Marco Arese[1,2], Luca Tamagnone[5,6], Donatella Valdembri[1,2‡], Massimo Santoro[3‡*] and Guido Serini[1,2‡*]

[1]*Candiolo Cancer Institute - FPO, IRCCS, Candiolo (TO), 10060, Italy*

[2]*Department of Oncology, University of Torino School of Medicine, Candiolo (TO), 10060 Italy*

[3]*Department of Biology, University of Padova, Padova, 35131, Italy*

[4]*Department of Molecular Biotechnology and Health Sciences, Molecular Biotechnology Center, University of Torino, 10126, Italy*

[5]*Institute of Histology and Embryology, School of Medicine, Catholic University of the Sacred Heart, Roma, 00168, Italy*

[6] *"Agostino Gemelli" University Polyclinic Foundation, IRCCS, Roma, 00168, Italy*

[†] Present address: Department of Surgery, Columbia University, New York, NY 10032, USA
[‡] These authors contributed equally to this work as senior authors.
[*] To whom correspondence should be addressed: guido.serini@ircc.it or massimo.santoro@unipd.it

SUMMARY

Dynamic modulation of endothelial cell (EC) adhesion to extracellular matrix (ECM) in response to mechanostimuli is essential for blood vessel patterning and functioning. Yet, the molecular mechanisms involved in this biological process are far to be completely deciphered. Here, we identify the adhesion G protein-coupled receptor (ADGR) Latrophilin 2 (LPHN2) as a novel determinant of vascular morphogenesis and endothelial barrier function. In cultured ECs, endogenous LPHN2 localizes at ECM adhesions, signals through cAMP/Rap1, and, *via* its fibronectin-leucine-rich transmembrane (FLRT)-binding domain, negatively regulates ECM-elicited haptotaxis. ECs also express endogenous FLRT2 ligand that promotes cAMP/Rap1 signaling and hinders haptotaxis in a LPHN2-dependent manner. Vascular ECs of *lphn2a* knock-out zebrafish embryos become abnormally stretched, display a hyperactive Hippo mechanosensing pathway, and lack proper intercellular junctions. Indeed, intravascularly injected cancer cells extravasate more easily in *lphn2a* null animals. Thus, LPHN2 ligands, such as FLRT2, may be therapeutically exploited to interfere with cancer metastatic dissemination.

KEYWORDS

Angiogenesis, Vascular permeability, Cancer, Guidance cues, Mechanosensing, Hippo pathway, G protein coupled receptors

INTRODUCTION

The small GTPase Rap1 (Wang *et al*, 2012) is known for its ability to drive vascular morphogenesis (Chrzanowska-Wodnicka, 2013) and to exert opposite effects on cell adhesion and motility (Coló *et al*, 2012; Hong *et al*, 2007; Lagarrigue *et al*, 2016; Lagarrigue *et al*, 2015; Lyle *et al*, 2008), likely because of the involvement of different subcellular pools of Rap1 regulators and effectors (Bos & Pannekoek, 2012). For instance, the Rap1-GTP-interacting adapter molecule (RIAM) can either promote, through talin, the conformational activation of integrin adhesion receptors at the leading edge of migrating cells (Lagarrigue *et al.*, 2016) or favor, via the mitogen-activated protein kinase kinase MEK, the disassembly of centrally located focal adhesions (FAs) (Coló *et al.*, 2012). Furthermore, major repulsive guidance cues such as secreted class 3 Semaphorins control blood vessel patterning (Valdembri *et al*, 2016; Wälchli *et al*, 2015) through the cytosolic GTPase activating protein domain of Plexin receptors (Worzfeld *et al*, 2014) that negatively regulates Rap1 signaling (Gioelli *et al*, 2018; Wang *et al.*, 2012). On the contrary, GPCRs promote Rap1 GTP loading *via* different pathways, the adenylyl cyclase (AC)/cyclic adenosine monophosphate (cAMP)/exchange protein directly activated by cAMP (EPAC) guanine nucleotide exchange factor cascade being a foremost one (Algire, 1943; Chang *et al*, 2007). However, cAMP/EPAC/Rap1 activation by different GPCRs also inhibits EC motility (Avanzato *et al*, 2016; Hong *et al.*, 2007).

To identify novel guidance receptors that, because of their ability to modulate endothelial Rap1 function, may play key roles in the regulation of vascular morphogenesis, we sought to focus on ADGRs that interact with several extracellular matrix (ECM) ligands and integrin receptors (Langenhan *et al*, 2013), whose adhesive functions are regulated by prototypic guidance cues such as Semaphorins that signal *via* Plexin receptors (Serini *et al*, 2003; Worzfeld & Offermanns, 2014). In this context, LPHN2 emerged as an ideal candidate because, similarly to Plexins, it was originally identified as a neuronal receptor (Südhof, 2001) and its

mRNA was reported to be highly expressed in *ex vivo* isolated blood vascular, but not lymphatic ECs (Valtcheva *et al*, 2013).

RESULTS AND DISCUSSION

To characterize the mechanisms by which endogenous LPHN2 protein controls ECM-driven EC directional migration, we investigated its subcellular localization and function in cultured human EC. First, we confirmed that LPHN2 protein is expressed on the surface of human ECs (**Fig. S1A**) and fluorescence confocal microscopy experiments revealed a strong enrichment of endogenous LPHN2 in vinculin containing ECM adhesions of ECs (**Fig. 1A**). Due to autocatalytic processing, ADGRs exist as noncovalently associated heterodimers comprising an extracellular and a transmembrane subunit (Langenhan *et al.*, 2013). To verify the relationships of both LPHN2 subunits with ECM adhesions, we transfected ECs with an N-terminally HA-tagged and C-terminally EGFP-tagged mouse Lphn2 construct (HA-Lphn2-EGFP; **Fig. S1B**). We found that, similarly to endogenous LPHN2, both the extracellular and the intracellular moieties of HA-Lphn2-EGFP co-localized with vinculin at cell-to-ECM adhesion sites (**Fig. 1B**). Next, we evaluated the outcome of LPHN2 silencing (**Fig. S2A**) on the ECM-elicited migration of ECs. Impedance-based time-lapse haptotaxis assays revealed that LPHN2 silenced (siLPHN2) ECs display a much faster directional motility towards type I collagen (Coll I) (**Fig. 1C**) or fibronectin (FN) (**Fig. S2B**) than control silenced (siCTL) ECs. Thus, in cultured ECs LPHN2 mediates inhibitory signals that are likely initiated by autocrine loops of endogenous LPHN2 ligands.

Several GPCRs activate the cAMP/Rap1 pathway that regulates cell adhesion and migration (Gloerich & Bos, 2011). Thus, we assessed whether in ECs LPHN2 may impact on basal cAMP production and Rap1 GTP loading by pulling it down with a glutathione-S-transferase (GST) fusion protein carrying the Rap1-binding domain of human Ral guanine

nucleotide dissociation stimulator (Franke *et al*, 1997). Compared to siCTL ECs, siLPHN2 ECs showed a decrease in the basal amount of both cAMP (**Fig. 1D**) and active Rap1 (**Fig. 1E**) by 52.6 ± 8.7% (n= 9; p≤ 0.001) and 36.35 ± 4.8% (n= 5; p≤ 0.001), respectively. Moreover, the introduction of a silencing resistant mouse Lphn2 construct (**Fig. S2C**) effectively rescued active Rap1 levels in siLPHN2 ECs (**Fig. 1E**). These findings were consistent with the notion that cAMP/EPAC/Rap1 activation can inhibit migration by modulating cell adhesion dynamics (Lyle *et al.*, 2008). Therefore, we next evaluated the impact of LPHN2 silencing on FAs and the associated F-actin stress fibers. Confocal microscopy analysis revealed that in ECs the lack of LPHN2 results in a significant increase in the number of vinculin-containing FAs (by 125.0 ± 32.1% vs. siCTL; n= 40 cells per experimental group in 5 independent experiments; p≤ 0.01) and F-actin stress fiber corrected total cell fluorescence (CTCF; by 107.5 ± 21.9 % vs. siCTL; n= 40 cells per experimental group in 4 independent experiments; p≤ 0.01) (**Fig. 1F**). The small GTPase RhoA controls stress fiber formation and FA turnover (Lawson & Burridge, 2014), and ADGRs, such as GPR56/ADGRG1, were previously reported to activate Rho GTPase (Paavola & Hall, 2012). However, we did not detect any reduction in Rho activation after LPHN2 silencing in ECs (**Fig. S2D**). Hence, LPHN2 activates cAMP/Rap1 signaling and negatively regulates both FA number and haptotactic cell migration in a RhoA-independent manner in ECs.

We reasoned that the higher migration rate caused by LPHN2 silencing in ECs (**Fig. 1C** and **Fig. S2B**) may be due to a loss of cell responsivity to LPHN2 ligands endogenously produced by ECs themselves, such as FLRT1-3 proteins (Seiradake *et al*, 2016). Indeed, the ectodomains of transmembrane FLRTs (Jackson *et al*, 2016) can be shed and act *in vivo* as repulsive factors capable of steering both axons (Yamagishi *et al*, 2011) and blood vessels (Seiradake *et al*, 2014). By means of real-time quantitative reverse transcription PCR (qRT-PCR) analysis, we observed that cultured human umbilical vein ECs actively transcribe *FLRT2*,

but neither *FLRT1* nor *FLRT3* genes (**Fig. 2A**). In addition, we found that LPHN2 silencing results in a two-fold upregulation of *FLRT2* mRNA in ECs (**Fig. 2B**), hinting that *FLRT2* and *LPHN2* gene transcription are reciprocally regulated. To investigate the potential role of FLRT2 binding in the inhibitory activity of LPHN2 on EC migration, we generated a mouse Lphn2 construct devoid of the olfactomedin domain (ΔOLF Lphn2; **Fig. 2C**), which mediates the binding of FLRT ligands to LPHN receptors (Seiradake *et al.*, 2016). Accordingly, ligand-receptor *in situ* binding assay on COS-7 cells demonstrated that FLRT2 interacts with high affinity with wild type (WT), but not ΔOLF Lphn2 (**Fig. 2C**). Next, we compared the abilities of WT and ΔOLF Lphn2 constructs to rescue the increased haptotactic migration of siLPHN2 ECs (**Fig. 2D**). Since WT, but not ΔOLF Lphn2 rescued the abnormal haptotaxis of siLPHN2 ECs (**Fig. 2D**), we concluded that LPHN2 inhibition of ECM-elicited EC motility relies on the binding of its olfactomedin domain to endogenous ligands, such as FLRT2. Consistently, haptotaxis assays showed that ECM-elicited EC directional migration is respectively increased upon silencing of endogenous FLRT2 (siFLRT2; **Fig. S3A, B**) (**Fig. 3A**) and decreased by stimulation with exogenous recombinant FLRT2 protein, which acts *via* LPHN2 (**Fig. 3B**). In agreement to what we observed upon LPHN2 silencing (**Fig. 1D-E**), siFLRT2 ECs displayed a decrease of the basal amount of both cAMP (**Fig. 3C**) and active Rap1 (**Fig. 3D**) by 12.9 ± 2.9 % (n= 6; $p \leq 0.05$) and 35.1 ± 6% (n= 4; $p \leq 0.01$) respectively, compared to siCTL ECs. In addition, stimulation with exogenous FLRT2 rescued active Rap1 GTP-loading in siFLRT2 ECs (**Fig. 3D** and **Fig.S3B**). Furthermore, confocal microscopy analyses revealed that, compared to siCTL ECs, siFLRT2 ECs display a substantially higher number of vinculin$^+$ FAs (by 108.07 ± 28.8 % vs. siCTL; n= 60 cells per experimental group in 4 independent experiments; $p \leq 0.05$) and F-actin stress fiber corrected total cell fluorescence (CTCF; by 99.9 ± 32.3 % vs. siCTL; n= 69 cells per experimental group in 4 independent experiments; $p \leq 0.05$) (**Fig. 3E**). Therefore, FLRT2 is one of the endogenous ligands sustaining autocrine LPHN2-

mediated chemorepulsive signals that negatively regulate the formation of FAs and associated and F-actin stress fibers in ECs.

In agreement with what we (**Fig. 1A** and **Fig.S1A**) and others (Valtcheva *et al.*, 2013) observed in cultured ECs, we found that Lphn2a protein is enriched in vascular ECs of dorsal aorta (DA) and posterior cardinal vein (PCV; **Fig. 4A**) of developing transgenic *Tg(kdrl:EGFP)*^{s843} zebrafish embryos. Hence, to directly investigate the functional role of LPHN2 in the *in vivo* vasculature, we generated a CRISPR/Cas9-mediated *lphn2a* zebrafish knock-out embryos with *Tg(kdrl:EGFP)*^{s843} genetic background (**Fig. S4**). The loss of Lphn2a did not grossly affect vascular patterning or blood circulation (**Fig. 4B**). However, we noticed that ECs forming the trunk vasculature were much thinner and stretched along the main vascular axis in *lphn2a*$^{-/-}$ than in wild type embryos (**Fig. 4B,** *lower panels*). To better characterize this aberrant vascular phenotype, we examined EC morphology of *lphn2a* zebrafish mutants by means of transmission electron microscopy (TEM) on ultra-thin cross-sections (**Fig. 4C**). TEM analyses of DA of 48 hours post-fertilization (hpf) of *lphn2a*$^{-/-}$ zebrafish embryos unveiled how, despite a normal vascular lumen, the lining ECs are extremely thin and devoid of properly organized tight junctions (TJs), compared to wild type animals (**Fig. 4C**). Thus, LPHN2 signaling drives EC morphogenesis and adhesion in living blood vessels.

Next, we further characterized the molecular mechanisms involved in the control of EC shape and adhesion by LPHN2 in developing embryonic blood vessels. In agreement with what observed in cultured human ECs (**Fig. 2A-B**), real time qRT-PCR confirmed that, also *in vivo*, the *flrt2* gene is actively transcribed in ECs sorted from wild type zebrafish embryos and *flrt2* mRNA levels significantly increase upon *lphn2a* gene knock-down (**Fig. S5**). *In vitro*, siLPHN2 ECs display a greatly increased number of FAs coupled to F-actin filaments (**Fig. 1**), which are known to function as mechanical sensors promoting the translocation of the Hippo

pathway effectors and transcriptional co-activators YAP and TAZ into the nucleus (Totaro *et al*, 2018; Yu *et al*, 2015). Indeed, in ECs plated on hydrogels with a soft (5kPa) elastic module, we found that LPHN2 silencing significantly increases YAP and TAZ nuclear translocation along with the transcription of YAP/TAZ target genes *CTGF* and *CYR61* (**Fig. S6**). Moreover, *in vivo* YAP/TAZ control EC shape and the formation of well-organized TJs (Kim *et al*, 2017), both of which we found to be altered in *lphn2a* null zebrafish embryos (**Fig. 4C**). Therefore, we assessed the impact of *lphn2a* knockdown on the activation of the Hippo pathway in ECs by exploiting the *Tg(Hsa.CTGF:nlsmCherry)*^{ia49}/ *Tg(kdrl:EGFP)*^{s843} double transgenic zebrafish fluorescent reporter line of Yap1/Taz activity (Astone *et al*, 2018). Of note, *lphn2a* null embryos displayed a significantly increased Yap1/Taz activation in vascular ECs (**Fig. 4D**) and moreover real-time qRT-PCR analysis revealed a robust upregulation of *ctgfa* and *cyr61* target gene mRNAs in *lphn2a*$^{-/-}$ sorted ECs compared to controls (**Fig. 4E**). Altogether, our findings support a model in which FLRT2-activated LPHN2 GPCR controls physiological vascular morphogenesis and endothelial barrier maturation by inhibiting EC-to-ECM adhesion and YAP/TAZ-mediated mechanotransduction.

The entry and exit of solutes, leukocytes, and cancer cells from the bloodstream is regulated by the endothelial barrier that relies on the controlled remodeling of intercellular junctions (Wettschureck *et al*, 2019). Since we found that the lack of Lphn2a results in the abnormal organization of TJs between ECs *in vivo* (**Fig. 4C**), we sought to investigate the impact of LPHN2 on the extravasation of cancer cells that can be effectively tracked and quantified by using the zebrafish embryo (Follain *et al*, 2018; Osmani & Goetz, 2019). To this aim, fluorescently-labeled mouse (B16F10) or human (SK-MEL-28) melanoma cells were injected in the duct of Cuvier of *Tg(kdrl:EGFP)*^{s843} wild type or *lphn2a*$^{-/-}$ zebrafish embryos and their metastatic extravasation potential was quantified by measuring the number of tumor cells outside the vessels in the caudal plexus where the circulating tumor cells (CTCs)

preferentially arrested and extravasated (Follain *et al.*, 2018; Hyenne *et al*, 2019). We discovered that, likely due to their abnormal inter-EC junctions, *lphn2a* null zebrafish embryos are more permissive to extravasation of both mouse B16F10 (**Fig. 5A**) and human SK-MEL-28 (**Fig. 5B**) melanoma cells compared to wild type embryos.

To conclude, we identified the endothelial ADGR LPHN2 as a novel repulsive guidance receptor that controls *in vivo* vascular morphogenesis and function. Our *in vitro* data suggest that, upon activation by ligands, such as FLRT2, LPHN2 elicits the synthesis of cAMP and Rap1-GTP pools that, in turn, may promote the turnover and keep the homeostatic balance in the number of ECM adhesions in vascular ECs. Our findings support the concept that, similarly to Rho small GTPases (Pertz, 2010), Rap1 is functionally organized into qualitatively distinct spatiotemporal signaling modules, which, at different subcellular locations and through distinct effectors, can elicit opposite effects. Indeed, Rap1 was described to both promote (Lagarrigue *et al.*, 2016; Lagarrigue *et al.*, 2015) and inhibit (Coló *et al.*, 2012; Hong *et al.*, 2007; Lyle *et al.*, 2008) cell adhesion and motility. It is conceivable that, based on its positioning at the leading edge or in centrally located mature adhesion sites Rap1-GTP may respectively signal to support ECM adhesion formation or turnover.

We also uncovered that LPHN2 signals by inhibiting the Hippo effectors YAP and TAZ in vascular ECs, both *in vitro* and *in vivo*. Although other GPCRs were described to modulate YAP/TAZ activation *via* Rho GTPase-regulated F-actin dynamics (Totaro *et al.*, 2018; Yu *et al.*, 2015), we did not detect any effect of LPHN2 silencing on Rho activation. The inhibition of the formation of FAs and F-actin stress fibers that we report here appears as the most conceivable mechanism by which LPHN2 negatively regulates YAP/TAZ signaling in ECs. In agreement with what previously reported [reviewed in (Park & Kwon, 2018)], the aberrant hyperactivation of YAP/TAZ caused by *lphn2a* knockdown in zebrafish embryos is associated with TJ disarrangement in blood vessel ECs. Our data show that, likely due to the loosening of

endothelial intercellular adhesions, the lack of Lphn2a might favor tumor melanoma cells extravasation. Such findings indicate that LPHN2 ligands, *e.g.* FLRT2, might be therapeutically exploited to strengthen the vascular barrier and to counteract cancer cell metastatic dissemination.

MATERIALS AND METHODS

DNA constructs

Mouse hemagglutinin (HA) tagged Lphn2 construct was synthesized by GeneArt Gene Synthesis (Thermo Fisher Scientific) and cloned into the Gateway system pENTR221 vector (Thermo Fisher Scientific). HA-Lphn2 cDNA was then subcloned into the pEGFP-N1 (Enhanced Green Fluorescent Protein (EGFP)) mammalian expression vector by standard PCR protocols. HA-Lphn2 ΔOLF pEGFP-N1 mutant construct lacking the Olfactomedin domain (amino acids 142-398) was obtained by PCR, according to the Taq polymerase manufacturer's instructions, using Phusion Site-Directed Mutagenesis Kit (Thermo Fisher Scientific). HA-Lphn2 WT and ΔOLF were also subcloned into the pCCL.sin.cPPT.polyA.CTE.eGFP.minhCMV.hPGK.Wpre (pCCL) lentiviral vector. Lentiviral particles were produced as described previously described (Gagliardi *et al*, 2012).

Cell culture

Primary human ECs were isolated from the umbilical cords as previously described (Jaffe *et al*, 1973). Briefly, umbilical vein was cannulated with a blunt 17-gauge needle that was secured by clamping. The umbilical vein was then perfused with 50 ml of phosphate-buffered saline (PBS) to wash out the blood. Next, 10 ml of 0.2% collagenase A (Cat. # 11088793001, Roche Diagnostics) diluted in cell culture medium were infused into the umbilical vein and incubated 30 min at room temperature. The collagenase solution containing the ECs was flushed from the cord by perfusion with 40 ml of PBS, collected in a sterile 50 ml centrifuge tube, and centrifuged 5 min at 800 *g*. Cells were first resuspended in M199 medium completed with cow brain extract, heparin sodium salt from porcine intestinal mucosa [0,025 mg/500 ml], penicillin/streptomycin solution, 20% fetal bovine serum (FBS) (Sigma Aldrich), and subsequently plated in cell culture dishes that had been previously adsorbed with 1% gelatin

from porcine skin (G9136, Sigma Aldrich). Cells were tested for mycoplasma contamination by means of Venor GeM Mycoplasma Detection Kit (MP0025-1KT, Sigma Aldrich) and grown in M199 complete medium. The isolation of primary venous ECs from human umbilical cords was approved by the Office of the General Director and Ethics Committee of the Azienda Sanitaria Ospedaliera Ordine Mauriziano di Torino hospital (protocol approval no. 586, Oct 22 2012 and no. 26884, Aug 28 2014) and informed consent was obtained from each patient. COS-7 (ATCC code CRL-1651) and HEK 293T cells were grown in DMEM medium completed with glutamine, penicillin/streptomycin solution, and 10% FBS (Sigma Aldrich). Both COS-7 and HEK 293T were transfected by means of Lipofectamine and PLUS reagent (Thermo Fisher Scientific). The calcium phosphate transfection method was instead used to transfect WT or ΔOLF Lphn2-HA-pCCL in HEK 293T cells and to produce the corresponding viral particles subsequently employed to transduce ECs.

Antibodies and reagents

2Y4824 rabbit polyclonal antibody (pAb) anti-LPHN2 was produced by Eurogentec by immunizing animals with peptide GGKTDIDLAVDENGL (amino acids 259-274)(Herberth *et al*, 2005). Rabbit 2Y4824 anti-LPHN2 was diluted 1:300 for immunofluorescence analysis. 2Y4824 rabbit anti-pre-immune serum (PIS; Eurogentec) was used for control purposes. Mouse monoclonal antibody (mAb) anti-HA tag (clone F-7), used 1:200 for immunofluorescence analysis, was from Santa-Cruz Biotechnology. Mouse mAbs anti-Vinculin (hVIN-1) and anti-α tubulin (clone B-5-1-2) were from Sigma-Aldrich and were diluted 1:400 and 1:8000 for immunofluorescence and Western blot analyses respectively. Rat mAb anti-HA High Affinity (clone 3F10), was from Roche and it was diluted 1:1000 for Western blot analysis. Mouse mAb anti-6xHis tag (clone HIS.H8) was from OriGene

Technologies. Goat pAb anti-FLRT2 (AF2877), from R&D Systems, was diluted 1:100 and 1:1000 for immunofluorescence and Western blot analysis, respectively.

Horseradish peroxidase (HRP) conjugated donkey anti-goat (sc-2056), goat anti-rabbit (sc-2054) and goat anti-rat secondary Abs were from Santa Cruz Biotechnology, while HRP-goat anti-mouse (115-035-003) was from Jackson ImmunoResearch Laboratories. Alexa Fluor 555 donkey anti-mouse (A31570), Alexa Fluor 555 donkey anti-rabbit (A31572), Alexa Fluor 555 Phalloidin (A34055), Alexa Fluor 488 donkey anti-rabbit (A21206) and donkey anti-goat (A11055), Alexa Fluor 647 donkey anti-mouse (A31571), and DAPI (D3571) were from Thermo Fisher Scientific. Alkaline phosphatase (AP)-labeled goat anti-mouse IgG (H+L) cross-adsorbed secondary Ab (G-21060) was from Thermo Fisher Scientific.

Uncropped scans of all blots are provided as Figures S7 and S8.

Recombinant proteins

Human fibronectin was from R&D Systems. Coll I from calf skin was produced by Sigma-Aldrich. Recombinant human carrier-free FLRT2 protein (2877-FL) was from R&D Systems. Streptavidin-conjugated HRP was from GE Healthcare.

Gene silencing in cultured ECs

The day before oligofection, ECs were seeded in six-well plates at a concentration of 12 x 10^4 cells per well. Oligofection of siRNA duplexes was performed according to the manufacturer's protocols. Briefly, human ECs were transfected twice (at 0 and 24 h) with 200 pmol of siGENOME Non-Targeting siRNA #1 (as control) or siGENOME SMART pools siRNA oligonucleotides (GE Healthcare Dharmacon), using Oligofectamine Transfection Reagent (Thermo Fisher Scientific). 24 h after the second oligofection, ECs were lysed or tested in functional assays. Knockdown of LPHN2 was achieved through the siGENOME SMART pool

siLPHN2 M-005651-02, while, in the case of FLRT2, was the siGENOME SMART pool siFLRT2 M-009104-00.

Western Blot analysis

Cells were lysed in buffer containing 25 mM Tris–HCl pH 7.4, 100 mM NaCl, 5% glycerol, 0.5 mM EGTA, 2 mM $MgCl_2$, 1 mM PMSF, 1 mM Na_3VO_4, protease inhibitor cocktail (Sigma Aldrich) and detergent 1% NP40. Cellular lysates were incubated for 20 min on ice, and then centrifuged at 15,000 *g*, 20 min, at 4 °C. The total protein amount was determined using the bicinchoninic acid (BCA) protein assay reagent (Thermo Fisher Scientific). Specific amounts of protein were separated by SDS–PAGE with precast Bolt 4-12% Bis-Tris gel (Thermo Fisher Scientific) or Mini PROTEAN TGX precast 7,5% gel (Bio-Rad). Proteins were then transferred to a nitrocellulose membrane (Bio-Rad), probed with Abs of interest and detected by enhanced chemiluminescence technique (PerkinElmer).

Immunoprecipitation

To immunoprecipitate and analyze by Western blot endogenous LPHN2, 5 x 10^6 HUVEC were transferred to ice, washed 3 times in cold PBS 1X, and surface-labeled at 4 °C with 0,2 mg/ml sulfo-NHS-SS-biotin (Thermo Scientific) in PBS1X for 30 min. Cells were then washed 3 times and lysed with a buffer containing 25 mM Tris–HCl pH 7.4, 100 mM NaCl, 1% Triton X-100, 5% glycerol, 0.5 mM EGTA, 2 mM $MgCl_2$, 1 mM PMSF, 1 mM Na_3VO_4, and protease inhibitor cocktail (Sigma Aldrich). Cellular lysates were incubated for 20 min on ice and then centrifuged at 15,000 *g*, 20 min, at 4 °C. The total protein amount was determined using the bicinchoninic acid (BCA) protein assay reagent (Thermo Fisher Scientific). Equivalent amounts (1 mg) of protein were precipitated for 1 h at 4 °C with protein A-Sepharose beads and then centrifuge for 1 min 15,000 *g* at 4 °C. Protein A-Sepharose beads were collected to

prepare the pre-clearing sample and the lysate were then immunoprecipitated for 1 h at 4 °C with the rabbit pAb anti-LPHN2 or pre-immune serum. Immunoprecipitates were washed four times with lysis buffer and then separated by SDS–PAGE. Proteins were then transferred to a nitrocellulose membrane (Bio-Rad), probed with Abs of interest and detected by enhanced chemiluminescence technique (PerkinElmer).

Rap1 and Rho-GTP pull-down assay

Rap1-GTP and Rho-GTP were respectively analyzed by means of the active Rap1 (Cat. #16120, Thermo Fisher Scientific) and Rho (Cat. #16116, Thermo Fisher Scientific) pull-down and detection kits. The assays were performed according to manufacturer's protocols. Total Rap1 or Rho proteins, detected in the input fractions, were used to calculate the normalized amount of active Rap1-GTP or active Rho-GTP. Bands were quantified with ImageJ software and normalized optical density (N.O.D.) was calculated relative to control.

Confocal scanning microscopy on cultured ECs

Cells were plated on 0.17 mm glass coverslips (no. 1.5) pre-coated with FN [5 μg/ml] and allowed to adhere for 3 h. Cells were washed in phosphate-buffered saline (PBS), fixed in 4% or 2% para-formaldehyde (PFA), permeabilized in 0.1% Triton or Saponin 0,01% PBS 1X for 2 min or 5 min on ice respectively, incubated with different primary Abs and revealed by appropriate Alexa-Fluor-tagged secondary Abs (Thermo Fisher Scientific). Cells were analyzed by using a Leica TCS SPEII confocal laser-scanning microscope (Leica Microsystems) employing the Leica LAS AF software for image acquisition. The acquisition was performed by adopting a laser power, gain, and offset settings that allowed maintaining pixel intensities (gray scale) within the 0–255 range and hence avoid saturation. Analysis of confocal images (Fig. 1F and 3E) was performed using the ImageJ software package. The

fluorescence intensity of F-actin has been calculated measuring the corrected total cell fluorescence (CTCF) parameter: CTCF = Integrated Density – (Area of selected cell x Mean fluorescence of background readings) (Gavet & Pines, 2010). FA number was measured applying for each cell a default threshold; moreover, FA number was normalized on cell area. Nuclear/cytoplasmic YAP and TAZ ratios were calculated by measuring the mean intensity fluorescence of each protein coming from the nucleus (overlapping with the DAPI staining) divided by its cytoplasmic localization (cell area – DAPI signal).

Binding assays

Empty vector, WT Lphn2 and ΔOLF Lphn2 expression constructs were transfected in COS-7cells to be used in the binding assay. *In situ* binding assays were performed as described previously (Tamagnone *et al*, 1999). Briefly, Lphn2-expressing COS-7 cells were incubated for 1h at 37° with or without recombinant 6xHis-tagged human FLRT2, mouse mAb anti-6xHis, and AP-labeled goat anti-mouse. After five washes in DMEM diluted 1:2 in PBS, cells were fixed and incubated with the AP substrate nitro blue tetrazolium–5-bromo-4-chloro-3-indolyl-phosphate (NBT–BCIP; Promega).

Haptotactic endothelial cell migration assays

Real time directional EC migration of ECs was monitored with an xCELLigence RTCA DP instrument (ACEA Biosciences). The bottom side of the upper chamber (the side facing the lower chamber) of CIM-Plate 16 was coated with 30 µl of 1 µg/ml Coll I or 3 µg/ml FN for 30 min at room temperature. Each lower chamber well was first filled with 160 µl of M199 1% FBS (containing or not 800 ng/ml of rhFLRT2 protein) and then assembled to the upper chamber. Each upper chamber well was then filled with 30 µl of M199 1% FBS. The plate was put for 1h at 37°C. The experiment file was set up using the RTCA Software 1.2. ECs were

detached and resuspended to a final concentration of 30,000 cells/100 µl. The BLANK step was started to measure the background impedance of cell culture medium, which was then used as reference impedance for calculating CI values. 100 µl of cell suspension (30,000 cells) were then added to each well of the upper chamber. The CIM-Plate 16 was placed in the RTCA DP Instrument equilibrated in a CO_2 incubator. ECs migration was continuously monitored using the RTCA DP instrument. Average, standard deviation and p value were calculated on the CI data exported from RTCA instrument for the technical replicates of each experimental condition in the time. Migration data are represented as a percentage considering the control samples as 100%.

cAMP assay

The cellular amounts of cAMP were quantified by using the non-acetylated cyclic AMP competitive ELISA Kit (Thermo Scientific, Cat. #EMSCAMPL) following to the manufacturer's instructions. The concentration of cAMP in samples was expressed as pmol of cAMP per mg of total proteins.

mRNA isolation from cultured ECs and real-time RT-PCR analysis

Cells were washed three times with PBS and frozen at -80°C. RNA isolation and reverse transcription: cells were thawed on ice, total RNA was extracted following the manufacturer's recommended protocol (ReliaPrep RNA Miniprep Systems, Promega. Cat. # Z6011). The quality and integrity of the total RNA were quantified by the NanoDrop 1000 spectrophotometer (Thermo Scientific). cDNAs were generated from 1 µg of total RNA using the High Capacity cDNA Reverse Transcription Kit (Applied Biosystems). TaqMan real-time RT-PCR assay: mRNA expression of *LPHN2*, *FLRT1-3*, and endogenous housekeeping control genes, *i.e.* glyceraldehyde 3-phosphate dehydrogenase (*GAPDH*), and TATA binding protein

(*TBP*), was measured by real-time RT-PCR using TaqMan Gene Expression Assays run on a C1000 Touch thermal cycler (Bio-Rad). The following assays were used: Hs00202347_m1 (*LPHN2*), Hs00534771_s1 (*FLRT1*), Hs00544171_s1 (*FLRT2*), Hs01922255_s1 (*FLRT3*), Hs00170014_m1 (*CTGF*), Hs00155479_m1 (*CYR61*), Hs99999905_m1 (*GAPDH*), and Hs00427620_m1 (*TBP*). For each sample, three technical replicates of each gene were run in a 96-well plate (cDNA concentration 50 ng/well) according the manufacturer's protocol. Between the two measured housekeeping genes, we chose a normalization factor calculation based on the geometric mean of *GAPDH* and *TBP* gene transcript for most of real-time RT-PCR experiments, while *GAPDH* only was employed in Fig.2A (Vandesompele *et al*, 2002). The experimental threshold (Ct) was calculated using the algorithm provided by the Bio-Rad CFX Manager 3.1 software (Bio-Rad). Ct values were converted into relative quantities using the method described by Pfaffl (Pfaffl, 2001) and amplification efficiency of each gene was calculated using a dilution curve and the slope calculation method (Pfaffl, 2001).

Zebrafish embryo lines and handling

Zebrafish were handled according to established protocols and maintained under standard laboratory conditions. Experimental procedures related to fish manipulation followed previously reported recommendations (Workman *et al*, 2010) and conformed to the Italian regulations for protecting animals used in research, including DL 116/92. The Ethics committee of the University of Torino approved this study. Larvae were anesthetized and then sacrificed by ice chilling. Following zebrafish lines were used for these studies: wild-type AB, *Tg(kdrl:EGFP)*^{s843} and *Tg(Hsa.CTGF:nlsmCherry)*^{ia49}/*Tg(kdrl:EGFP)*^{s843}.

Generation of *lphn2a* null zebrafish embryos

Lphn2a$^{-/-}$ zebrafish mutants were generated by CRISPR/Cas9-mediated genome editing at ZeClinics (Barcelona, Spain). A single guide RNA (sgRNA) was designed using the online tool http://crispor.tefor.net/, based on exon site, high efficacy, and not off-target published algorithms to specifically target an optimal CRISPR sequence on exon 2 of *lphn2a* gene (ENSDARG00000069356). The *lphn2a*-targeting sgRNA, with the specific targeting sequence CAACCGTCAAGACGAATACA-AGG, was injected in one-cell stage embryos in a solution containing Nls-CAS9 protein (PNA BIO). The mutagenesis efficacy was evaluated on pools of 30 injected embryos, whose genomic DNA was PCR amplified and analyzed via T7 endonuclease system. F_0 injected embryos were raised to adulthood and screened, by genotyping the F_1, for germline transmission of the mutation. Heterozygous mutants harboring the mutation were then incrossed to obtain homozygous mutants (F5 generation). The genomic region surrounding the CRISPR target site was PCR-amplified using the following primers: *lphn2a*-Fw (5'- TCTCAGAGTGACTTCCCCGGATC -3'), *lphn2a*-Rv (5'- GCAGCCATTATTTATCCCAGCTACC -3'). *Lphn2a*$^{-/-}$ heterozygous and homozygous mutants were identified by analyzing in agarose gel the PCR product digested with TasI restriction enzyme (TSP509I, Thermo Fisher Scientific) and by sequencing.

Transmission electron microscopy (TEM)

Embryos were anaesthetized and fixed with 2.5% glutaraldehyde in 0.1 M sodium cacodylate buffer, then dehydrated, embedded in epoxy resin and sectioned, following a standard TEM sample preparation protocol (Santoro *et al*, 2009). All steps after fixation were performed by the TEM service of the Department of Biology (University of Padova, Italy).

Larvae dissociation and fluorescence activated cell sorting (FACS)

Wild type and *Tg(kdrl:EGFP)*^{s843} larvae at 2 days post-fertilization (dpf) were dissociated as previously described (Zancan *et al*, 2015) using 1x PBS, 0.25% trypsin phenol red free, 1 mM EDTA pH 8.0, 2.2 mg/ml Collagenase P (Sigma). Digestion was stopped by adding $CaCl_2$ to a final concentration of 1 mM and fetal calf serum to 10%. Dissociated cells were rinsed once in PBS and resuspended in Opti-MEM (Gibco), 1% fetal calf serum and 1X Penicillin-Streptomycin solution (Sigma). Cells were filtered through a 40 µm nylon membrane. For sorting, we used FACS Aria IIIu sorter (BD Biosciences, San José, USA) with the following settings for EGFP: argon-ion Innova Laser (Coherent, USA) (488 nm, 100 mW); 100 µM nozzle; sorting speed 500 events/s in 0-32-0 sort precision mode. We performed data acquisition and analysis with the BD FACSDiva software (BD Biosciences, San José, CA, USA). GFP^+ and GFP^- cells were separately collected in resuspension medium, and RNA was extracted using the RNA isolation kit Nucleospin® RNA XS (Macherey-Nagel). cDNA was made with RT High Capacity kit (Applied Biosystems) according to the manufacturer's protocol. Quantitative real-time RT-PCR on ECs from zebrafish was performed with CFX384 Touch Real-time PCR Detection System (Biorad) using 5x HOT FIREPol®EvaGreen® qPCR Mix Plus (Solis BioDyne), the following primer sequences were used *lphn2*-F: 5'-AGTATCCCTCATCTGCCTGG-3' *lphn2*-R: 5'-AGCTGAACTCCTTCCAGACA-3'; *flrt2*-F: CATTGCATGGCTCAGGTCTC, *flrt2*-R: ATGAGTTGGCCAGGGATGAA, *cyr61*-F: 5'-GCGGAGACTCGGAGAAAGAAC-3', *cyr61*-R 5'-CGATGCACTTCTCCATCTGATG3'; *ctgfa*-F: 5'-CTCCCCAAGTAACCGTCGTA-3', *ctgfa*-R: 5'-CTACAGCACCGTCCAGACAC-3; *ctgfb*-F: 5'-CCCACAAGAAGACACCTTCC-3', *ctgfb*-R: 5'-ATTCGCTCCATTCAGTGGTC-3'. Results are expressed as relative mRNA abundance and normalized to actin beta1 (*actb1*) or eukaryotic translation elongation factor 1 alpha 1, like 1 (*eef1a1l1*) as endogenous reference genes, which were amplified by employing the following

primer sequences *actb1*-F: 5' GTATCCACGAGACCACCTTC-3', *actb1*-R: 5'-GAGGAGGGCAAAGTGGTAAAC-3'; *eef1a1l1*-F 5'-GACAAGAGAACCATCGAG-3', *eef1a1l1*-R 5'-CCTCAAACTCACCGACAC-3'.

Intravascular injection of cancer cells in zebrafish embryos

At 48 hpf, embryos were dechorionated at 2 dpf, anesthetized with tricaine 0.16 mg/ml and placed along plastic lanes immersed in 2% methylcellulose/PBS. Sub-confluent cells in 10cm culture dishes were rinsed twice with warm serum free medium and then incubated for 30 minutes at 37°C (B16F10 or SK-MEL28) with MemBright-560 (Lipilight-IDYLLE) and quickly diluted in serum free medium (200nM final). To eliminate all possible traces of unbound MemBright-560, cells were then rinsed three times with serum free medium, then with EDTA, and trypsinized. Stained cells (at $100 \cdot 10^6$ cells per ml) were loaded in a glass capillary needle and microinjected into the duct of Cuvier of the embryos under the stereomicroscope using a WPI PicoPump apparatus. Xenotransplanted embryos were grown at 32° C, monitored daily and analyzed starting from one day post injection (dpi) up to 3 days.

Images acquisition and analysis on zebrafish embryos

Double transgenic fluorescence of *Tg(kdrl:EGFP)*^{s843} and Tg *(Hsa.CTGF:nlsmCherry)*in *lphn2a*$^{-/-}$ mutant background was visualized under a AZ100 stereomicroscope equipped with AxioCam (Zeiss) dissecting microscope and then with a Leica SP8 confocal microscope. Larvae were anaesthetized and mounted in 1% low-melting- point agarose gel. Endothelial cells targeted EGFP and nuclear mCherry fluorescence (Yap/Taz) was visualized by using 488 nm and 561 nm lasers. All images were analyzed with Fiji software (https://fiji.sc/). Yap/Taz signal were automatically segmented on the mCherry fluorescence image stacks, inside a EGFP fluorescent mask identifying endothelial cells, and total signal intensity was calculated,

according to previous work (Facchinello *et al*, 2016). After confocal acquisition, heterozygous and homozygous siblings were genotyped by PCR on DNA previously extracted from a single larva, as described by (Gagnon *et al*, 2014).

Statistical analysis

For statistical evaluation of *in vitro* experiments, parametric two-tailed heteroscedastic Student's t test was used to assess the statistical significance when two groups of unpaired normally distributed values were compared; when more than two groups were compared, parametric two-tailed analysis of variance (ANOVA) with Bonferroni's post hoc analysis was applied; with the only exception for Fig. 2A, all bar plots represent relative values of the corresponding control.

For statistical evaluation of *in vivo* experiments, neither randomization nor blinding was applied for samples or zebrafish embryo analyses. No statistical method or criteria was used to predetermine sample size or to include/exclude samples or animals. The Shapiro-Wilk normality test was used to confirm the normality of the data. The statistical difference of Gaussian data sets was analyzed using the Student unpaired two-tailed t test, with Welch's correction in case of unequal variances. For data not following a Gaussian distribution, the Mann-Whitney test was used. Illustrations of statistical analyses of *in vivo* experiments are presented as the means ± SEM.

ACKNOWLEDGEMENTS

We are grateful to Alberto Puliafito for help with data analysis. The research leading to these results has received funding from: Fondazione AIRC IG grants #13016, #16702, and #21315 (to G.S.), #19923 (to L.T.), #20366 (to D.V.), and #20119 (to M.M.S.); Fondazione AIRC under 5 per Mille 2018 - ID. 21052 program – P.I. Comoglio Paolo, G.L. Tamagnone Luca, G.L. Serini Guido, ; FPRC-ONLUS Grant "MIUR 2010 Vaschetto - 5 per mille 2010 MIUR" (to G.S.); Telethon Italy (GGP09175) (to G.S.); Associazione ‘Augusto per la Vita’ (to G.S.); ERC-CoN project 647057 - rEnDOx (to M.M.S.).

AUTHOR CONTRIBUTIONS

G.S. conceived the project; G.S., C.C., M.M.S., and N.F. designed the experiments; G.S., C.S., D.V., and M.M.S. supervised the research; L.T. and M.A. provided key reagents, methods, and technologies; C.C., N.F., D.G., G.V. and N.G. performed the experiments; C.C., N.F., D.G., G.V., N.G., C.S., D.V., M.A., L.T., M.M.S., and G.S. analyzed the data; C.C., N.F., D.G., G.V., N.G., C.S., D.V., M.A., L.T., M.M.S., and G.S. interpreted the results; C.C., N.F., M.M.S., and G.S. wrote the paper; all authors read and approved the manuscript.

CONFLICT OF INTEREST

Authors declare no conflict of interest

REFERENCES

Algire GH (1943) Microscopic Studies of the Early Growth of a Transplantable Melanoma of the Mouse, Using the Transparent-chamber Technique. *J Natl Cancer Inst* 4: 13-20

Astone M, Lai JKH, Dupont S, Stainier DYR, Argenton F, Vettori A (2018) Zebrafish mutants and TEAD reporters reveal essential functions for Yap and Taz in posterior cardinal vein development. *Sci Rep* 8: 10189

Avanzato D, Genova T, Fiorio Pla A, Bernardini M, Bianco S, Bussolati B, Mancardi D, Giraudo E, Maione F, Cassoni P *et al* (2016) Activation of P2X7 and P2Y11 purinergic receptors inhibits migration and normalizes tumor-derived endothelial cells via cAMP signaling. *Sci Rep* 6: 32602

Bos JL, Pannekoek WJ (2012) Semaphorin signaling meets rap. *Sci Signal* 5: pe6

Chang YS, Kim HJ, Chang J, Ahn CM, Kim SK (2007) Elevated circulating level of osteopontin is associated with advanced disease state of non-small cell lung cancer. *Lung Cancer* 57: 373-380

Chrzanowska-Wodnicka M (2013) Distinct functions for Rap1 signaling in vascular morphogenesis and dysfunction. *Exp Cell Res* 319: 2350-2359

Coló GP, Hernández-Varas P, Lock J, Bartolomé RA, Arellano-Sánchez N, Strömblad S, Teixidó J (2012) Focal adhesion disassembly is regulated by a RIAM to MEK-1 pathway. *J Cell Sci* 125: 5338-5352

Facchinello N, Schiavone M, Vettori A, Argenton F, Tiso N (2016) Monitoring Wnt Signaling in Zebrafish Using Fluorescent Biosensors. In: *Wnt Signaling*, Barrett Q.L., Lawrence (ed.) pp. 81-94. Humana Press: New York, NY

Follain G, Osmani N, Azevedo AS, Allio G, Mercier L, Karreman MA, Solecki G, Garcia Leòn MJ, Lefebvre O, Fekonja N *et al* (2018) Hemodynamic Forces Tune the Arrest, Adhesion, and Extravasation of Circulating Tumor Cells. *Dev Cell* 45: 33-52.e12

Franke B, Akkerman JW, Bos JL (1997) Rapid Ca2+-mediated activation of Rap1 in human platelets. *EMBO J* 16: 252-259

Gagliardi PA, di Blasio L, Orso F, Seano G, Sessa R, Taverna D, Bussolino F, Primo L (2012) 3-phosphoinositide-dependent kinase 1 controls breast tumor growth in a kinase-dependent but Akt-independent manner. *Neoplasia* 14: 719-731

Gagnon JA, Valen E, Thyme SB, Huang P, Akhmetova L, Ahkmetova L, Pauli A, Montague TG, Zimmerman S, Richter C *et al* (2014) Efficient mutagenesis by Cas9 protein-mediated oligonucleotide insertion and large-scale assessment of single-guide RNAs. *PLoS One* 9: e98186

Gavet O, Pines J (2010) Progressive activation of CyclinB1-Cdk1 coordinates entry to mitosis. *Dev Cell* 18: 533-543

Gioelli N, Maione F, Camillo C, Ghitti M, Valdembri D, Morello N, Darche M, Zentilin L, Cagnoni G, Qiu Y *et al* (2018) A rationally designed NRP1-independent superagonist SEMA3A mutant is an effective anticancer agent. *Sci Transl Med* 10: eaah4807

Gloerich M, Bos JL (2011) Regulating Rap small G-proteins in time and space. *Trends Cell Biol* 21: 615-623

Herberth G, Stein A, Glienke J, Taudien S, Klaman I, Herr A, Thierauch K-H, Sommer A (2005) Human Latrophilin-2 is Expressed in the Cytotrophoblast and Syncytiotrophoblast of Placenta and in Endothelial Cells. *American Journal of Biochemistry and Biotechnology* 1: 135-144

Hong J, Doebele RC, Lingen MW, Quilliam LA, Tang WJ, Rosner MR (2007) Anthrax edema toxin inhibits endothelial cell chemotaxis via Epac and Rap1. *J Biol Chem* 282: 19781-19787

Hyenne V, Ghoroghi S, Collot M, Bons J, Follain G, Harlepp S, Mary B, Bauer J, Mercier L, Busnelli I *et al* (2019) Studying the Fate of Tumor Extracellular Vesicles at High Spatiotemporal Resolution Using the Zebrafish Embryo. *Dev Cell* 48: 554-572.e557

Jackson VA, Mehmood S, Chavent M, Roversi P, Carrasquero M, Del Toro D, Seyit-Bremer G, Ranaivoson FM, Comoletti D, Sansom MS *et al* (2016) Super-complexes of adhesion GPCRs and neural guidance receptors. *Nat Commun* 7: 11184

Jaffe EA, Nachman RL, Becker CG, Minick CR (1973) Culture of human endothelial cells derived from umbilical veins. Identification by morphologic and immunologic criteria. *J Clin Invest* 52: 2745-2756

Kim J, Kim YH, Park DY, Bae H, Lee DH, Kim KH, Hong SP, Jang SP, Kubota Y, Kwon YG *et al* (2017) YAP/TAZ regulates sprouting angiogenesis and vascular barrier maturation. *J Clin Invest* 127: 3441-3461

Lagarrigue F, Kim C, Ginsberg MH (2016) The Rap1-RIAM-talin axis of integrin activation and blood cell function. *Blood* 128: 479-487

Lagarrigue F, Vikas Anekal P, Lee HS, Bachir AI, Ablack JN, Horwitz AF, Ginsberg MH (2015) A RIAM/lamellipodin-talin-integrin complex forms the tip of sticky fingers that guide cell migration. *Nat Commun* 6: 8492

Langenhan T, Aust G, Hamann J (2013) Sticky signaling--adhesion class G protein-coupled receptors take the stage. *Sci Signal* 6: re3

Lawson CD, Burridge K (2014) The on-off relationship of Rho and Rac during integrin-mediated adhesion and cell migration. *Small GTPases* 5: e27958

Lyle KS, Raaijmakers JH, Bruinsma W, Bos JL, de Rooij J (2008) cAMP-induced Epac-Rap activation inhibits epithelial cell migration by modulating focal adhesion and leading edge dynamics. *Cell Signal* 20: 1104-1116

Osmani N, Goetz JG (2019) Multiscale Imaging of Metastasis in Zebrafish. *Trends Cancer* 5: 766-778

Paavola KJ, Hall RA (2012) Adhesion G protein-coupled receptors: signaling, pharmacology, and mechanisms of activation. *Mol Pharmacol* 82: 777-783

Park JA, Kwon YG (2018) Hippo-YAP/TAZ signaling in angiogenesis. *BMB Rep* 51: 157-162

Pertz O (2010) Spatio-temporal Rho GTPase signaling - where are we now? *J Cell Sci* 123: 1841-1850

Pfaffl MW (2001) A new mathematical model for relative quantification in real-time RT-PCR. *Nucleic Acids Res* 29: e45

Santoro MM, Pesce G, Stainier DY (2009) Characterization of vascular mural cells during zebrafish development. *Mech Dev* 126: 638-649

Seiradake E, del Toro D, Nagel D, Cop F, Härtl R, Ruff T, Seyit-Bremer G, Harlos K, Border EC, Acker-Palmer A *et al* (2014) FLRT structure: balancing repulsion and cell adhesion in cortical and vascular development. *Neuron* 84: 370-385

Seiradake E, Jones EY, Klein R (2016) Structural Perspectives on Axon Guidance. *Annu Rev Cell Dev Biol* 32: 28.21–28.32

Serini G, Valdembri D, Zanivan S, Morterra G, Burkhardt C, Caccavari F, Zammataro L, Primo L, Tamagnone L, Logan M *et al* (2003) Class 3 semaphorins control vascular morphogenesis by inhibiting integrin function. *Nature* 424: 391-397.

Südhof TC (2001) alpha-Latrotoxin and its receptors: neurexins and CIRL/latrophilins. *Annu Rev Neurosci* 24: 933-962

Tamagnone L, Artigiani S, Chen H, He Z, Ming GI, Song H, Chedotal A, Winberg ML, Goodman CS, Poo M *et al* (1999) Plexins are a large family of receptors for transmembrane, secreted, and GPI-anchored semaphorins in vertebrates. *Cell* 99: 71-80.

Totaro A, Panciera T, Piccolo S (2018) YAP/TAZ upstream signals and downstream responses. *Nat Cell Biol* 20: 888-899

Valdembri D, Regano D, Maione F, Giraudo E, Serini G (2016) Class 3 semaphorins in cardiovascular development. *Cell Adh Migr*: 1-11

Valtcheva N, Primorac A, Jurisic G, Hollmén M, Detmar M (2013) The orphan adhesion G protein-coupled receptor GPR97 regulates migration of lymphatic endothelial cells via the small GTPases RhoA and Cdc42. *J Biol Chem* 288: 35736-35748

Vandesompele J, De Preter K, Pattyn F, Poppe B, Van Roy N, De Paepe A, Speleman F (2002) Accurate normalization of real-time quantitative RT-PCR data by geometric averaging of multiple internal control genes. *Genome Biol* 3: RESEARCH0034

Wang Y, He H, Srivastava N, Vikarunnessa S, Chen YB, Jiang J, Cowan CW, Zhang X (2012) Plexins are GTPase-activating proteins for Rap and are activated by induced dimerization. *Sci Signal* 5: ra6

Wettschureck N, Strilic B, Offermanns S (2019) Passing the Vascular Barrier: Endothelial Signaling Processes Controlling Extravasation. *Physiol Rev* 99: 1467-1525

Workman P, Aboagye EO, Balkwill F, Balmain A, Bruder G, Chaplin DJ, Double JA, Everitt J, Farningham DA, Glennie MJ *et al* (2010) Guidelines for the welfare and use of animals in cancer research. *Br J Cancer* 102: 1555-1577

Worzfeld T, Offermanns S (2014) Semaphorins and plexins as therapeutic targets. *Nat Rev Drug Discov* 13: 603-621

Worzfeld T, Swiercz JM, Sentürk A, Genz B, Korostylev A, Deng S, Xia J, Hoshino M, Epstein JA, Chan AM *et al* (2014) Genetic dissection of plexin signaling in vivo. *Proc Natl Acad Sci U S A* 111: 2194-2199

Wälchli T, Wacker A, Frei K, Regli L, Schwab ME, Hoerstrup SP, Gerhardt H, Engelhardt B (2015) Wiring the Vascular Network with Neural Cues: A CNS Perspective. *Neuron* 87: 271-296

Yamagishi S, Hampel F, Hata K, Del Toro D, Schwark M, Kvachnina E, Bastmeyer M, Yamashita T, Tarabykin V, Klein R *et al* (2011) FLRT2 and FLRT3 act as repulsive guidance cues for Unc5-positive neurons. *EMBO J* 30: 2920-2933

Yu FX, Zhao B, Guan KL (2015) Hippo Pathway in Organ Size Control, Tissue Homeostasis, and Cancer. *Cell* 163: 811-828

Zancan I, Bellesso S, Costa R, Salvalaio M, Stroppiano M, Hammond C, Argenton F, Filocamo M, Moro E (2015) Glucocerebrosidase deficiency in zebrafish affects primary bone ossification through increased oxidative stress and reduced Wnt/β-catenin signaling. *Hum Mol Genet* 24: 1280-1294

Figure legends

Figure 1. LPHN2 concentrates at ECM adhesions and negatively regulates ECM-elicited EC haptotaxis. (**A**) Confocal microscopy analysis of ECs indicates how endogenous LPHN2, as detected by an anti-LPHN2 antibody (*green*), co-localizes with vinculin (*red*) in ECM adhesions of ECs as shown in merging (right panel). Lower row panels are magnifications of the corresponding upper row panels. Scale bar 20 μm. (**B**) Fluorescence confocal microcopy reveals that in ECs transfected with HA-Lphn2-EGFP both the extracellular, as detected by an anti-HA antibody (*red*), and the EGFP-fused intracellular (*green*) moieties co-localize with vinculin (*blue*) at ECM adhesions, as shown in merging (right panel). Lower row panels are magnifications of the corresponding upper row panels. Scale bar 20 μm. (**C**) Real time analysis of haptotactic migration control (siCTL) or LPHN2 (siLPHN2) silenced ECs toward Coll I was assessed with an xCELLigence RTCA DP system. Results are the average ± SEM of six independent assays. Statistical analysis: results were analyzed by a two-tailed heteroscedastic Student's t-test; $p \leq 0.001$ ***. (**D**) LPHN2 silencing in ECs decreases basal cAMP amount. siCTL and siLPHN2 absolute cAMP concentration values are 5.6 and 2.6 [pmol/ml] respectively. Results are the average ± SEM of nine independent assays. (**E**) LPHN2 silencing in human ECs decreases basal GTP loading of Rap1 small GTPase and pCCL lentivirus-mediated overexpression of silencing-resistant mouse Lphn2 rescues the decrease in Rap1-GTP levels. Total Rap1 was employed to calculate the normalized optical density (N.O.D.) levels of active Rap1-GTP. Results are the average ± SEM of five independent experiments, one of which is shown. Statistical analysis: parametric two-tailed analysis of variance (ANOVA) with Bonferroni's post hoc analysis; ANOVA p value <0.0001; Bonferroni's p value <0.0001 for CTL/siCTL vs. CTL/siLPHN2 and 0.0019 for CTL/siLPHN2 vs. Lphn2/siLPHN2. (**F**) Confocal microscopy analysis of endogenous LPHN2 (*green*), vinculin (*blue*), and phalloidin-labeled F-actin (*red*) reveals how, compared to siCTL ECs, LPHN2 silencing increases the number of vinculin-containing FAs and the amount of F-actin stress fibers (evaluated as CTCF) in siLPHN2 ECs. Lower row panels are magnifications of the corresponding upper row panels. Scale bars for siCTL panels and siLPHN2 panel are 10 μm

and 15 μm respectively. Results concerning the number of vinculin-containing FAs and the amount of F-actin stress fibers are the average ± SEM of five independent experiments for a total of 45 (siCTL) and 38 (siLPHN2) ECs and four independent experiments for a total of 54 (siCTL) and 36 (siLPHN2) ECs respectively. Statistical analysis: results were analyzed by a two-tailed heteroscedastic Student's t-test; p≤ 0,01 **. See also Figures S1 and S2.

Figure 2. FLRT2-binding OLF domain of LPHN2 is necessary to inhibit ECM-elicited EC motility. (**A**) Real time quantitative PCR analysis of *FLRT1-3* mRNAs in human ECs relative to the house keeping gene *GAPDH*. Results are the average ± SEM of four independent experiments (**B**) Real time quantitative PCR analysis of *LPHN2* and *FLRT1-3* mRNAs in siCTL and siLPHN2 human ECs. Results are normalized on siCTL values and are the average ± SEM of four independent experiments. Statistical analysis: results were analyzed by a two-tailed heteroscedastic Student's t-test; p≤ 0,01 **; p≤ 0,001 ***. (**C**) COS-7 cells transfected with empty vector or WT HA-Lphn2-EGFP or ΔOLF HA-Lphn2-EGFP constructs and their expression verified by Western blot analysis employing a rat mAb anti-HA. Next, COS-7 cells transfected with empty vector or WT HA-Lphn2-EGFP or ΔOLF HA-Lphn2-EGFP constructs were incubated or not with 6xHis-tagged rhFLRT2. The binding between the Lphn2 constructs and the rhFLRT2 ligand was revealed through sequential incubation with a mouse mAb anti-6xHis, an AP-conjugated goat anti-mouse pAb, and the AP substrate NBT–BCIP. Results show how WT, but not ΔOLF Lphn2 binds rhFLRT2. (**D**) Real time analysis of haptotactic EC migration toward Coll I was assessed with an xCELLigence RTCA DP system. Cells were first transduced with WT HA-Lphn2-pCCL, ΔOLF HA-Lphn2-pCCL and empty pCCL (CTL) lentiviral constructs and then oligofected with either siCTL or siLPHN2 siRNAs. Haptotactic migration toward Coll I of ECs was analyzed over time. SiLPHN2 ECs migrate faster in comparison to siCTL ECs and only transduction with WT, but not ΔOLF rescues the excessive migration siLPHN2 ECs. Results are the average ± SEM of three independent experiments. Results were analyzed by a two-tailed heteroscedastic Student's t-test comparing CTL/siCTL (*blue*) to CTL/siLPHN2 (*red*) and CTL/siLPHN2 to WT (*green*) or ΔOLF Lphn2/siLPHN2 (*purple*); p≤ 0,01 **; p≤ 0,001 ***. See also Figure S2.

Figure 3. FLRT2 negatively regulates ECM-elicited EC haptotaxis via LPHN2 and triggers cAMP/Rap1 signaling. (**A**, **B**) Real time analysis of haptotactic EC migration toward Coll I was assessed with an xCELLigence RTCA DP system. Statistical analysis: results were

analyzed by a two-tailed heteroscedastic Student's t-test; p≤ 0,05 *; p≤ 0,01 **; p≤ 0,001 ***. (**A**) Endogenous FLRT2 silencing (siFLRT2) increases haptotactic migration compared to siCTL ECs. Results are the average ± SEM of six independent assays. (**B**) Exogenous rhFLRT2 [800 ng/ml] inhibits siCTL, but not siLPHN2 EC haptotaxis. For sake of simplicity data from the same experiments are plotted in two separated graphs: siCTL (left graph) and siLPHN2 (right graph). Results are the average ± SEM of four independent assays. (**C**) Endogenous FLRT2 silencing in ECs decreases basal cAMP amount. siCTL and siFLRT2 absolute cAMP concentration values are 4.7 and 3.69 [pmol/ml] respectively. Results are the average ± SEM of seven independent assays. Statistical analysis: results were analyzed by a two-tailed heteroscedastic Student's t-test; p≤ 0,05 *. (**D**) Endogenous FLRT2 silencing (siFLRT2) in ECs decreases basal Rap1-GTP levels and treatment of siFLRT2 ECs with exogenous rhFLRT2 [800 ng/ml] rescues the decrease in Rap1-GTP levels. Total Rap1 was employed to calculate the normalized optical density (N.O.D.) levels of active Rap1-GTP. Results are the average ± SEM of four independent experiments, one of which is shown. Statistical analysis: parametric two-tailed analysis of variance (ANOVA) with Bonferroni's post hoc analysis; ANOVA p value 0.0019; Bonferroni's p value 0.0012 for siCTL vs. siFLRT2 and 0.0269 for siFLRT2 vs. siFLRT2 + FLTR2. (**E**) Confocal microscopy analysis of endogenous FLRT2 (*green*), vinculin (*blue*), and phalloidin-labeled F-actin (*red*) reveals how, compared to siCTL ECs, FLRT2 silencing increases the number of vinculin-containing FAs and the amount of F-actin stress fibers, evaluated as CTCF, in siFLRT2 ECs. Lower row panels are magnifications of the corresponding upper row panels. Scale bars for siCTL panels and siFLRT2 panel are 10 µm and 15 µm respectively Results concerning the number of vinculin-containing FAs and the amount of F-actin stress fibers are the average ± SEM of four independent experiments for a total of 63 (siCTL) and 59 (siFLRT2) ECs and four independent experiments for a total of 71 (siCTL) and 60 (siFLRT2) ECs respectively. Statistical analysis: results were analyzed by a two-tailed heteroscedastic Student's t-test; p≤ 0,05 *. See also Figure S3.

Figure 4. LPHN2 controls vascular morphogenesis and YAP/TAZ signaling in zebrafish embryo. (**A**) Confocal fluorescence microscopy analysis of trunk cross-sections at 72 hpf of *Tg*(*Kdrl:EGFP*)^{s843} zebrafish embryos carrying EC-specific EGFP expression. Lphn2 protein is enriched in ECs of dorsal aorta (DA) and posterior cardinal vein (PCV). Scale bar: 60 µm. (**B**) *Upper panels*. Lateral view in bright field and fluorescence confocal microscopy of wild type (WT) and CRISPR/Cas9-mediated *lphn2a* knock-out (*lphn2a*$^{-/-}$) zebrafish embryos in the

Tg(kdrl:EGFP)^{s843} background. Scale bars: 100 µm. See also Figure S3. *Lower panels*. Confocal images of the trunk region of wild type *lphn2a*$^{+/+}$ and CRISPR/Cas9-mediated *lphn2a* knock-out (*lphn2a*$^{-/-}$) zebrafish embryos in the *Tg(kdrl:EGFP)*^{s843} background with Color code images of endothelial shapes in the dorsal aorta and cardinal vein at 72 hpf from *lphn2a*$^{+/+}$ and *lphn2a*$^{-/-}$ zebrafish embryos in which profiles of ECs were automatically segmented on EGFP fluorescence confocal microscopy image stacks. Scale bars: 50 µm. (**C**) TEM analysis of WT and *lphn2a*$^{-/-}$ dorsal aorta (n=3) at 48 hpf. Scale bars: 1 µm (upper images) and 5 µm (lower images). EC: endothelial cells, L: lumen, red arrow: EC tight junctions. Color code identification of EC lumen. (**D**) Yap1/Taz reporter activity is prominent in the endothelium during development from 20 to 48 hpf. *Left panels*, Representative confocal images of *Tg(Hsa.CTGF:nlsmCherry)*^{ia49} /*Tg(kdrl:EGFP)*^{s843} double transgenic WT and *lphn2a*$^{-/-}$ siblings at 72hpf (n= 4). Yap1/Taz activation signal was automatically segmented on fluorescent confocal mCherry image Z-stacks, inside a EGFP fluorescent mask identifying endothelial cells, and only this endothelial cell-restricted Yap1/Taz signal intensity was calculated and represented in 3D analysis. Scale bars: 50 µm. *Right panel*, Relative quantification of integrated density of Yap1/Taz *Hsa.CTGF:nlsmCherry* reporter activity signal that co-localizes with *kdrl:GFP*. Statistical analysis: results were analyzed by a Mann-Whitney test; p≤ 0,05 *. (**E**) Real time quantitative PCR analysis of *ctgfa*, *ctgfb*, and *cyr61* mRNAs of FACS-sorted ECs isolated from *lphn2a*$^{+/+}$ or *lphn2a*$^{-/-}$ zebrafish embryos at 48 hpf relative to the house keeping gene *actb1* and normalized on the mRNA levels measured in *lphn2a*$^{+/+}$ animals. Results are the average ± SEM of ≥3 independent assays (n>80 embryos for condition). Statistical analysis: results were analyzed by a Mann-Whitney test; p≤ 0,001 ***. See also Figures S4, S5, and S6.

Figure 5. LPHN2 impairs cancer cell extravasation in zebrafish embryos. (**A, B**) MemBright-560-labeled melanoma cells were microinjected into the duct of Cuvier of 48 hpf *lphn2a*$^{+/+}$ or *lphn2a*$^{-/-}$ *Tg*(*Kdrl:EGFP*)^{s843} zebrafish embryos. After 36 hours, extravasated metastatic melanoma cells were imaged by confocal analysis of the caudal plexus. Mouse B16F10 (**A**, red) and human SK-MEL-28 (**B**, purple) melanoma cell extravasation is enhanced in *lphn2a*$^{-/-}$ compared to *lphn2a*$^{+/+}$ zebrafish embryos. Results are the average ± SEMA of 2 independent assays, in which 17 (B16F10) and 14 (SK-MEL-28) animals were analyzed. Scale bars: 50 µm. Statistical analysis: results were analyzed by a Mann-Whitney test; p≤ 0,05 *.

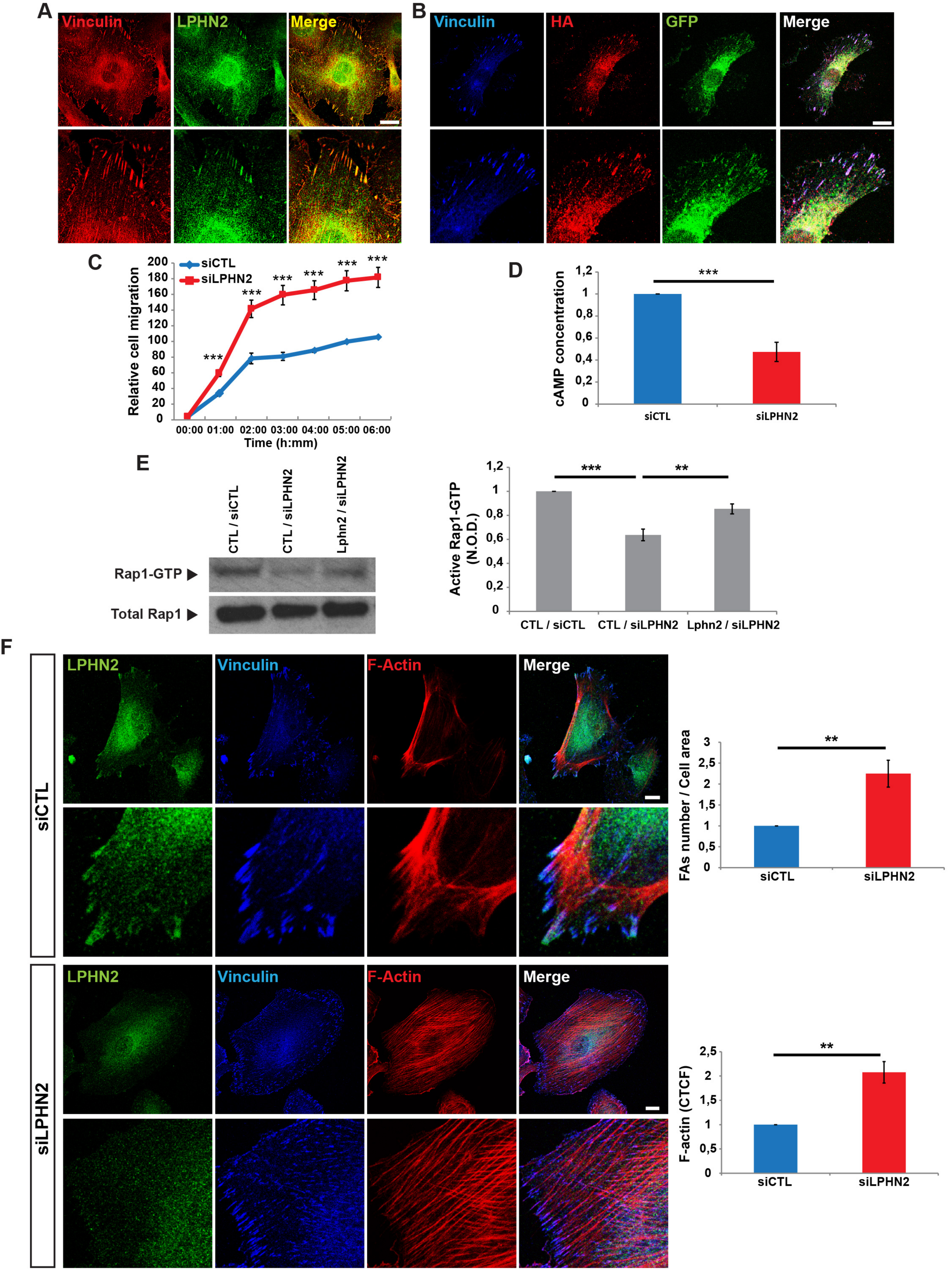

Camillo et al., Figure 1

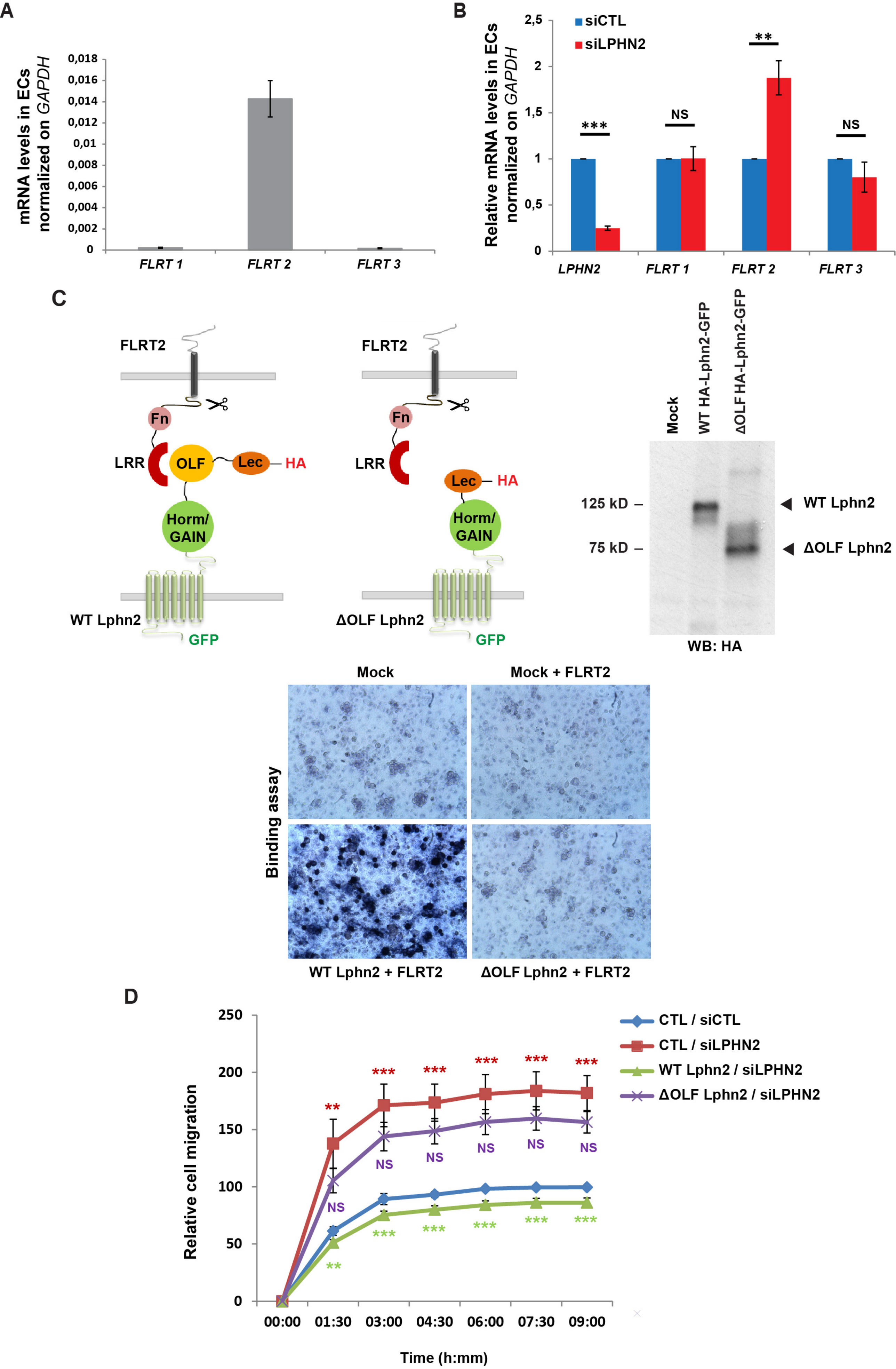

Camillo et al., Figure 2

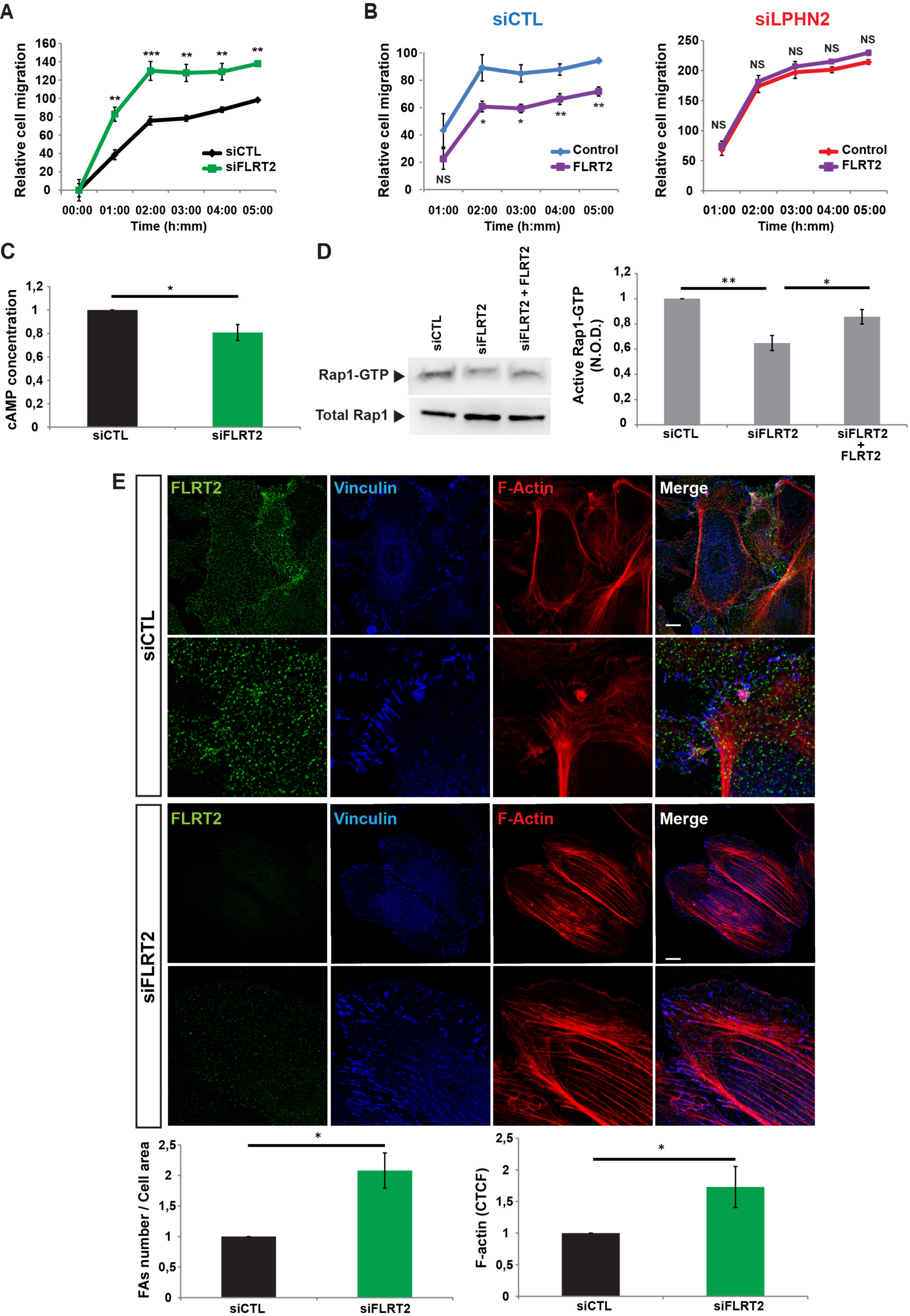

Camillo et al., Figure 3

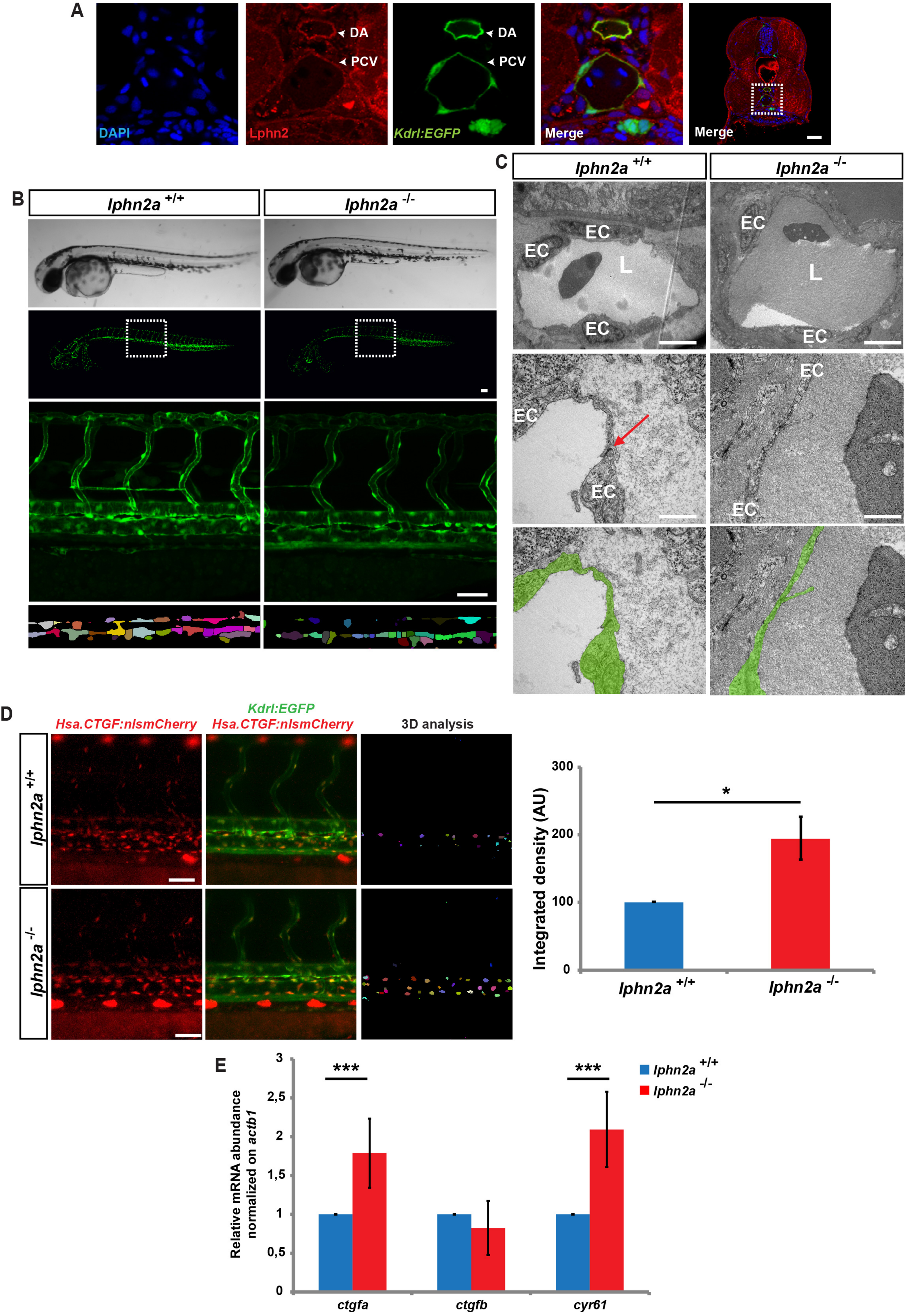

Camillo et al., Figure 4

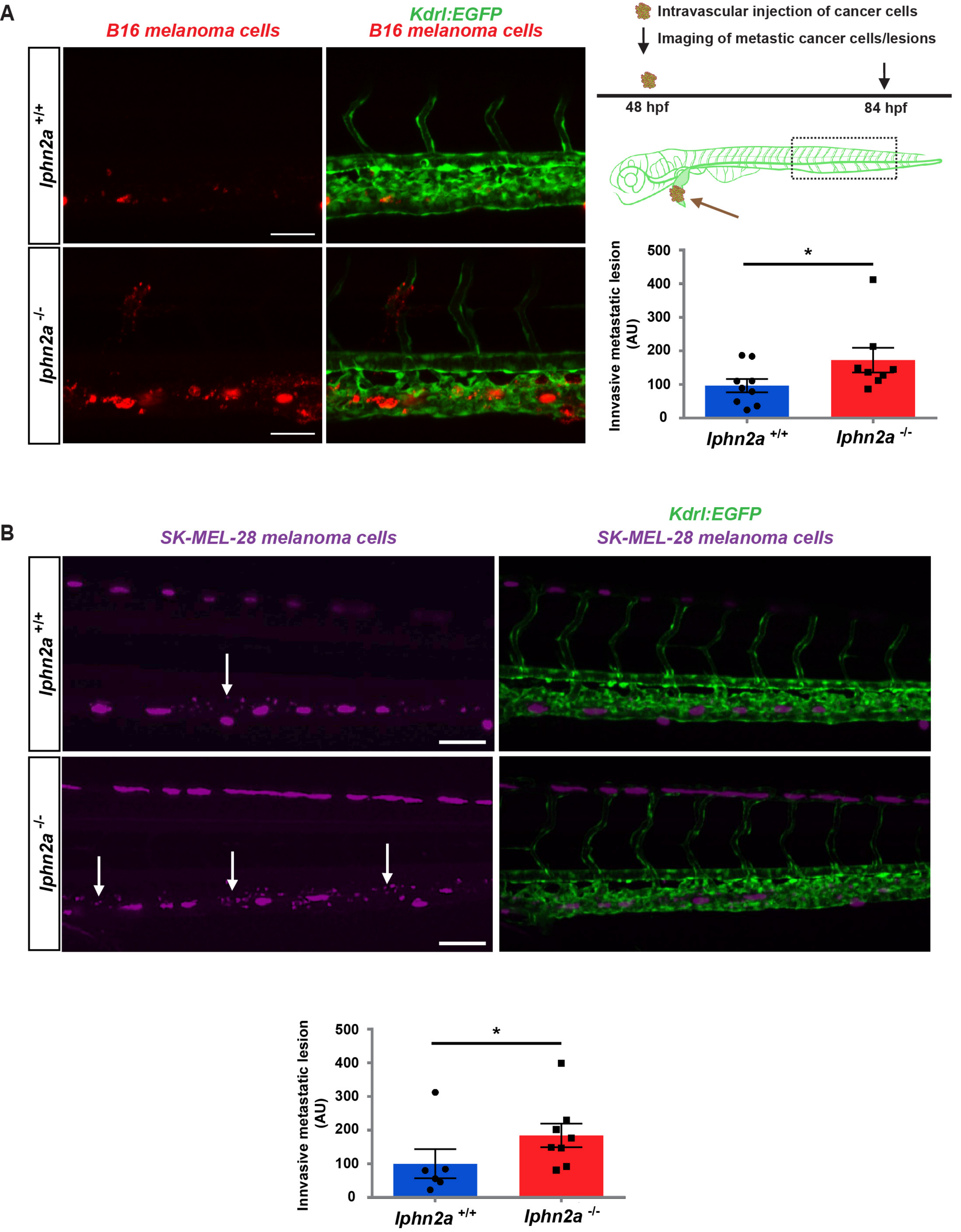

Camillo et al., Figure 5